کد مقاله: CCI2126

دومین کنفرانس احتراق ایران
بهمن ماه 1386 - مشهد- دانشگاه آزاد اسلامی مشهد

انجمن احتراق ایران

Modeling of chamber flowfield of solid rocket motors with erosive burning

M.A. Maneshian[1], M.H. Akbari[2]
Dept. of Mechanical Engineering, *Shiraz University*
Molla-Sadra Ave., Shiraz, 71348-5114, Iran
akbari@eng.shirazu.ac.ir

Abstract
The performance of a solid rocket motor depends heavily on the flow characteristics, the chemical composition of the grain, combustion products and the burning rate. In this study the start-up transient internal ballistics of a typical solid rocket motor (SRM) is numerically simulated. Two burning rate laws are used to model simple and erosive burning. Governing equations of 2-dimensional inviscid flow are solved using an explicit MacCormack finite difference technique in which the locations of shock waves are captured by the solution scheme. Erosive burning increases the chamber pressure and thrust during the early portion of burning for a particular motor.

Keywords: Solid rocket motor- Erosive burning- Euler equations- MacCormack scheme

1- Introduction
A solid rocket motor is the simplest form of chemical propulsion. The fuel and oxidizer are both incorporated in a single solid, called the propellant grain, located inside a container called the combustion chamber. The solid rocket motor belongs to the family of the rocket engine (thrust achieved by mass ejection) and its history can be considered both ancient and recent.

Preliminary prediction of SRM performance can be achieved using numerical simulation of its internal ballistics [1-2]. Due to recent progress in computing power this field is developing rapidly [3]. Better knowledge of internal flow field should make possible to optimize solid propellant grain geometries and thermal insulation thicknesses for efficient size and shape of the combustion chamber and exhaust nozzle [4].

In this paper we discuss details of a general code which simulates SRM with cylindrical grains. The motor configuration incorporates a very low port to throat area ratio, which in turn results in a very high velocity propellant gas traveling across burning propellant surface, particularly near the aft end of the propellant. This phenomenon is known as erosive burning. Erosive burning is defined as the increase in burning rate of a solid propellant that occurs as a function of hot gas cross-flow at the propellant surface [5]. The amount of burning rate increase is established by comparing the erosive burning rate to the burning rate that occurs at the same local pressure for no cross-flow. The primary mechanism for the increase in rate is the additional heat that is fluxed into the surface as a result of the cross-flow. Several factors contribute to this increase in heat flux, including the thermal gradient in the boundary layer, and turbulent enhancement of the local transport properties.

Several analytical and numerical studies of erosive burning have been conducted. Razdan and Kuo [6] used a turbulent boundary layer approach to show that the augmented burning rate with free stream velocity is due to the increased heat feedback and increase in transport coefficients, as well as increased turbulent mixing. Gordon, Duterque, and Lengelle [7] used a 1-D wall zone model coupled with a fully turbulent 2-D description of the whole flow field to develop an erosive burning model correlated to wall shear stress. They also concluded that the propellant's normal burning rate was the primary influence on the threshold for erosive burning. Bulgakov, and Karpov [8] also used the boundary layer equations to study the burning of stick propellant and negative erosive burning (a decrease in burning rate with blowing across the surface), and found satisfactory agreement with experimental data. Mukunda and Paul [9] conducted a study to examine the universal behavior of erosive burning. They concluded that for most practical propellants, erosive burning effects are primarily a function of the non-erosive mass flux and the Reynolds number, with little effect due to chemical kinetics.

Governing equations of an axisymmetric inviscid flow are solved using an explicit MacCormack finite difference technique in which the locations of shock waves are captured by the solution scheme. To evaluate performance of the present code, transient flow field of several SRMs with different burning surfaces are simulated.

---

[1] Graduate student
[2] Assistant professor and corresponding author

2- Numerical Model

Fig. 1 shows a typical SRM with inner burning surface. The mixture of the gases is assumed to be frozen in equilibrium and the reaction to be finished near the grain surface. Gas flow is assumed to be inviscid and unsteady. For many analysis problems in solid rocket motors, an assumption of inviscid flow provides sufficiently accurate results for design or development tasks [1-2]. Typically, this assumption results in an error of 0.2 to 0.7% [10].

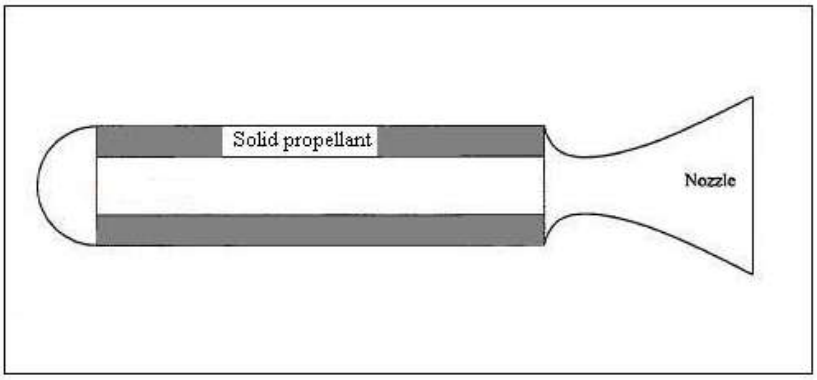

Fig. 1. Schematic of a solid rocket motor.

The governing equations in the conservative form are:

$$\frac{\partial U}{\partial t}+\frac{\partial F}{\partial r}+\frac{\partial G}{\partial z}+\frac{S}{r}=0 \tag{1}$$

where U represents the conserved variable solution vector

$$U=\left[\rho,\rho v_r,\rho v_z,E\right]^T \tag{2}$$

v_r and v_z are the radial and axial components of the gas velocity V, and E is the total energy per unit volume of the gas. The vectors F and G are the flux vectors in the r and z directions, respectively, and S represents the sources due to the axisymmetric flow geometry.

$$F=\begin{bmatrix}\rho v_r\\ \rho v_r^2+p\\ \rho v_r v_z\\ v_r(E+p)\end{bmatrix},\qquad G=\begin{bmatrix}\rho v_z\\ \rho v_r v_z\\ \rho v_z^2+p\\ v_z(E+p)\end{bmatrix},\qquad S=\begin{bmatrix}\rho v_r\\ \rho v_r^2\\ \rho v_r v_z\\ v_r(E+p)\end{bmatrix} \tag{3}$$

The gas-phase is taken to be calorically perfect and the total energy is then given by

$$E=\frac{p}{(\gamma-1)}+\frac{\rho}{2}(V\cdot V) \tag{4}$$

where γ is the ratio of the specific heats for the gas flow. Expressions for the overall propellant burning rate are intrinsically coupled to the gas dynamic flow equations, and these equations must be defined before the core flow can be computed. Two laws of burning rate are used: simple burning, Eq. 5, and Lenoir-Robillard erosive burning law [10], Eq. 6.

$$r_b=a_T\,p^n \tag{5}$$

$$r_b=a_T\,p^n+\frac{\alpha G^{0.8}}{D^{0.2}e^{(\beta\cdot r_b\rho_p/G)}} \tag{6}$$

where

$$\alpha=\frac{0.0288\,C_p\mu^{0.2}\,Pr^{-0.667}}{\rho_p\,C_{ps}}\left(\frac{T_f-T_s}{T_s-T_i}\right) \tag{7}$$

Here a_T stands for burning rate coefficient, n is the burning rate pressure exponent, G is mass flow velocity per unit area, D is characteristic dimension of port passage, ρ_p is the propellant density, β is a constant with a value of 53, c_p is the average specific heat of combustion gases, μ is gas viscosity, Pr is the Prandtl number, c_{ps} is the heat capacity of solid propellant, T_f is the flame temperature, T_s is the propellant surface temperature, and T_i is the initial ambient temperature within the propellant.

An explicit MacCormack finite difference technique is used to solve the equations. Finite difference methods are useful for complex equation sets such as the Euler or Navier-Stokes equations, but can be effectively used only in simple geometric regions. Using finite difference methods for complex geometries requires adopting coordinate systems or coordinate mappings which transform the physical domain into a computational domain of simple shape. In this paper, a set of simple analytical stretching functions are used to map the bounding surfaces into a square computational domain. Therefore physical plane (r,z,t) can be easily mapped onto planes or lines in the computational domain (η,ξ,τ) with a general transformation:

$$\begin{aligned}\xi &= \xi(r,z,t)\\ \eta &= \eta(r,z,t)\\ \tau &= t\end{aligned} \tag{8}$$

Formally applying the chain rule of change of independent variables for Eq. (1) results in the following conservation laws in the (ξ,η) plane

$$\frac{\partial \widetilde{E}}{\partial \tau}+\frac{\partial \widetilde{F}}{\partial \eta}+\frac{\partial \widetilde{G}}{\partial \xi}+S=0 \tag{9}$$

where

$$\widetilde{E}=JE,\qquad \widetilde{F}=JG\frac{\partial \xi}{\partial z}+JF\frac{\partial \xi}{\partial r},\qquad \widetilde{G}=JG\frac{\partial \eta}{\partial z}+JF\frac{\partial \eta}{\partial r},\qquad \widetilde{S}=JS \tag{10}$$

and J is the Jacobian of transformation.

The governing equations in the fluid domain are solved using a MacCormack scheme [11]. The basic scheme is an explicit, time marching scheme that produces second order time and space accuracy. The time derivative at each time step is first calculated by calculating the spatial derivatives with a first order forward scheme. The scheme can be extended to fourth order spatial accuracy by replacing the first order forward and backward terms with second order forward and backward schemes. The solution is temporarily advanced in time, where the time derivatives are then recalculated based on the new values and a first order backward scheme. The two time derivatives are averaged, and the solution is permanently advanced one time step. The scheme can be written symbolically as

(Predictor)

$$\widetilde{U}^{*}_{i,j}=\widetilde{U}^{n}_{i,j}-\frac{\Delta t}{\Delta \eta}(\widetilde{F}^{n}_{i+1,j}-\widetilde{F}^{n}_{i,j})-\frac{\Delta t}{\Delta \xi}(\widetilde{G}^{n}_{i,j+1}-\widetilde{G}^{n}_{i,j})-\Delta t\,\widetilde{S}^{n}_{i,j} \tag{11}$$

(Corrector)

$$\widetilde{U}^{n+1}_{i,j}=\frac{1}{2}\left[\widetilde{U}^{n}_{i,j}+\widetilde{U}^{*}_{i,j}-\frac{\Delta t}{\Delta \eta}(\widetilde{E}^{*}_{i,j}-\widetilde{E}^{*}_{i-1,j})-\frac{\Delta t}{\Delta \xi}(\widetilde{G}^{*}_{i,j}-\widetilde{G}^{*}_{i,j-1})-\Delta t\,\widetilde{S}^{*}_{i,j}\right] \tag{12}$$

Notice that the spatial derivatives are discretized with opposite one-sided finite differences in predictor and corrector stages. The star variables are supposed to be evaluated at time level t_{n+1}.

3- Initial and Boundary Conditions

Initial Conditions

At time $t=0$ velocity components v_r and v_z are everywhere set to zero, and pressure and temperature are set to the ambient values everywhere in the flow field. Density and internal energy are obtained from the equations of state. Boundary conditions must also be specified for all of the dependent variables v_r, v_z, ρ, E along with corresponding values of p and T.

Boundary Conditions

Four types of boundary conditions are required for the computation of the flow field, i.e. wall, inflow, outflow and symmetry conditions. They are prescribed as follows. On the impermeable wall, slip conditions are specified along with an adiabatic wall for gas phase. On the symmetry line, the normal velocity of gas phase and the gradients in the normal direction of all other variables are specified as zero.

Propellant surface boundary conditions**:**

The gas velocity boundary condition should be divided into two cases: burning surface and unburning surface. For the velocity on a unburning surface, the following relation is given: $v_r = v_z = 0$.

For the velocity of a burning surface the normal velocity is given by:

$$v_r = \frac{\rho_p}{\rho_g} r_b \tag{13}$$

If the flow is subsonic at nozzle exit, the atmospheric condition is adopted; otherwise the solution is extrapolated at the exit.

Two cases are simulated in the present study. The first case is to validate the present code by comparing the results with those presented in [12] for a similar motor under similar operating conditions. In the second case, simulation results for erosive and simple burning laws are compared with each other. The general configuration of the motor for the two cases is similar (Fig. 2), but the characteristics of the propellant, as well as the specific dimensions for the motor are different (Table 1). The nozzle used in these simulations has a cosine profile.

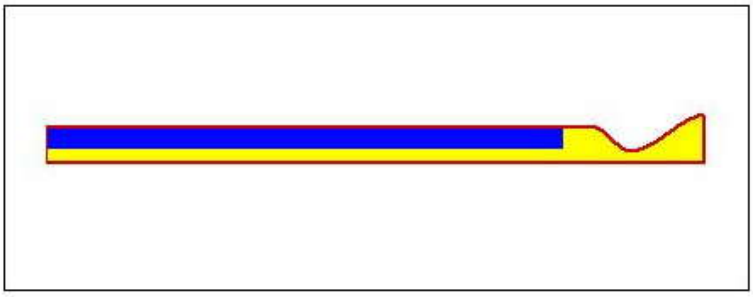

Fig. 2. Schematic illustration of the motor used in simulations.

Table 1. Characteristics of the motor.

Specification	**Present study**	**Used for comparison with [12]**
Chamber length (cm)	73.5	200
Propellant grain length (cm)	69.5	200
Inner radius of the grain (cm)	1.8	9
Outer radius of the grain (cm)	4.7	10
Nozzle expansion ratio	4.8	8
Nozzle total length (cm)	15	40
Nozzle diverging section length (cm)	10	30
Burning rate coefficient (a_T) cm/s	0.07	0.1
Burning rate exponent (n)	0.35	0.35
Propellant density (ρ_P) Kg/m^3	1730	1845
Propellant specific heat (C_{ps}) J/Kg K	1500	–
Propellant flame temperature (T_f) K	3000	2993
Propellant surface temperature (T_s) K	1000	–
Gas Prandtl number (Pr)	0.72	–
Specific gas constant (R) J/Kg K	320	323.75
Gas absolute viscosity (μ) Kg/m.s	8.075×10^{-5}	–

4- Numerical Results

In order to validate the code, various test problems were examined by the scheme. One such problem is the calculation of flow field through a converging-diverging nozzle with different back pressures and with and without shock. Good agreement with the exact solution has been achieved (Table 2, Fig. 3).

Table 2. The ratio of throat pressure to stagnation pressure.

Case	Exact Analytical Solution	Numerical Solution
$p_t/p_0 = 0.93$	0.627	0.632
$p_t/p_0 = 0.80$	0.528	0.530
$p_t/p_0 = 0.70$	0.528	0.530

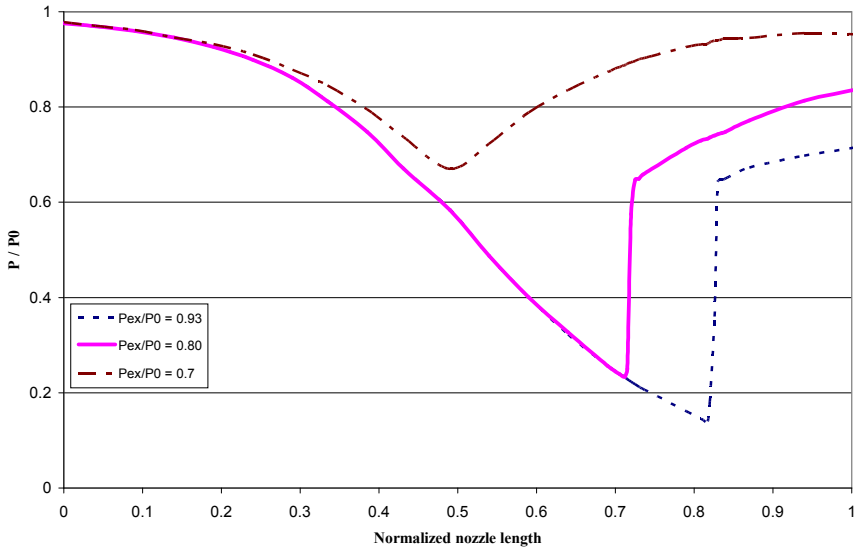

Fig.3. Pressure distribution through a converging-diverging nozzle as predicted by MacCormack method.

Comparison of the results obtained by present study and [11] also show the capability of the present code for the modeling of solid rocket motors. Fig. 4 shows the variation of the head end pressure with time for a specified motor used in [11]. It is noted that simple burning law is used in this simulation.

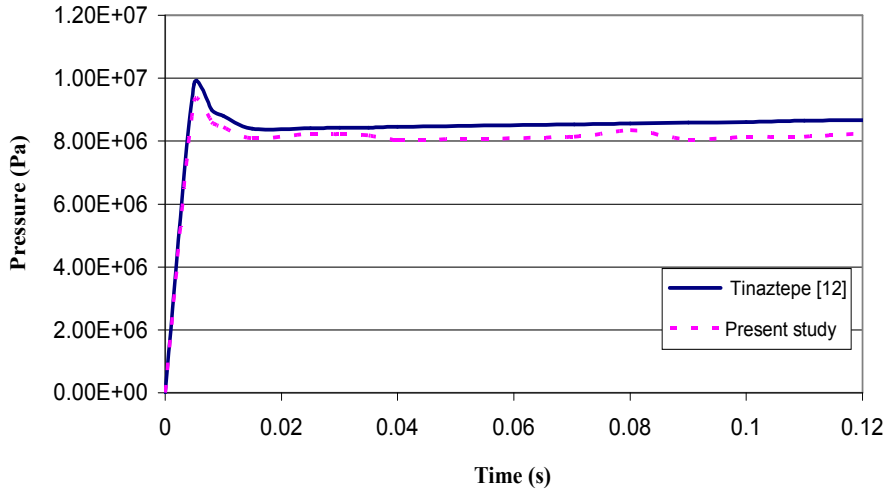

Fig. 4. Head-end pressure versus time; comparison of the present code with [12].

After obtaining a validated code for transient and steady-state solutions, ballistic calculations of a generic solid rocket motor was performed. The gird used for the computations has 566×70 nodes. Fig. 5 shows physical domain grid at the nozzle entrance region of the motor. Figs. 6 to 8 show the pressure contours at the motor head-end, aft end, and nozzle of the motor, respectively, for simple burning. It is clear that the maximum pressure is at the head-end of the motor while the minimum pressure occurs at the nozzle exit. Figs. 9 and 10 show head-end pressure and thrust versus time for simple and erosive burning. Erosive burning increases the burning rate, hence increasing the mass flow rate, and causing the pressure and thrust within the chamber to rise above those for the simple burning case.

A comparison of burning rates is highlighted in Fig. 11. When erosive burning is considered the burning rate becomes a function of both local pressure and local velocity. In this case the highest rate of burning is at the aft end of the grain. In simple burning, burning rate is only a function of the pressure. Therefore, the highest burning rate is at the head end of the grain which is the location of highest pressure.

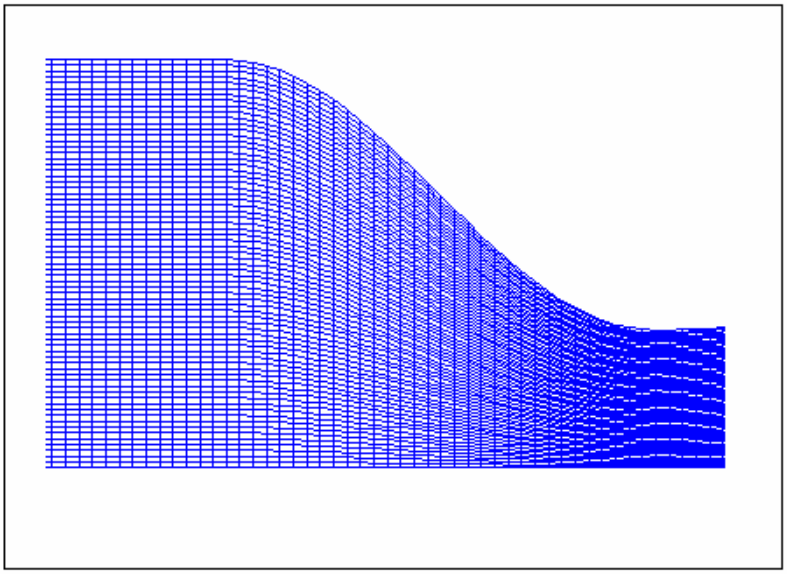

Fig.5. Physical domain grid at the nozzle entrance region.

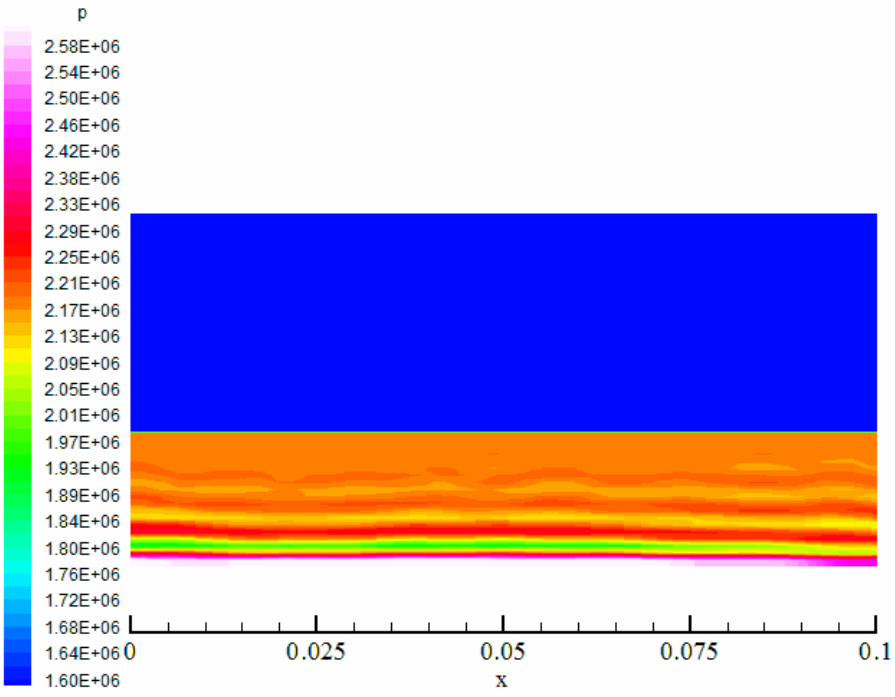

Fig.6. Pressure contours at the motor head-end (grain is identified by the low pressure region).

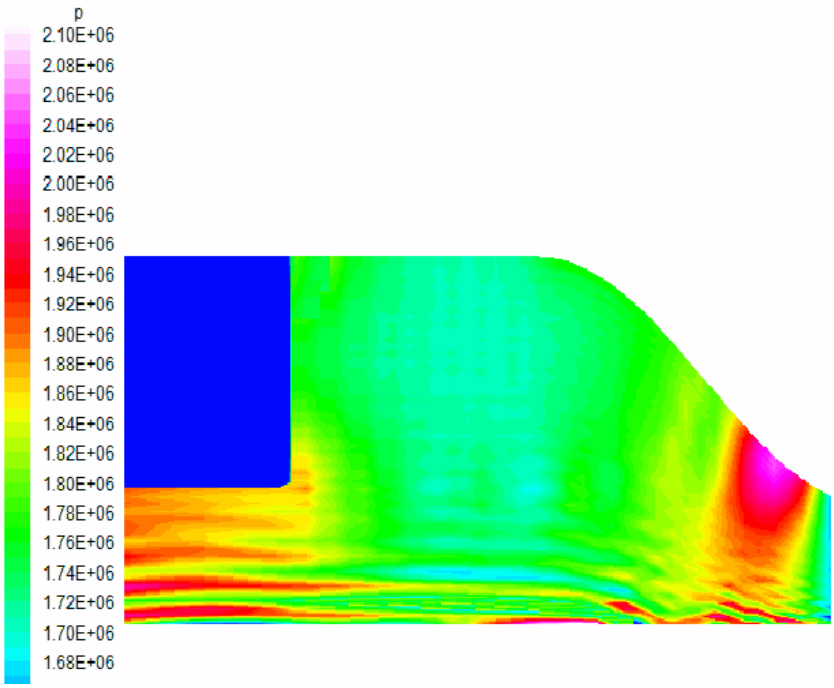

Fig.7. Pressure contours at the motor aft-end (grain is identified by the low pressure region).

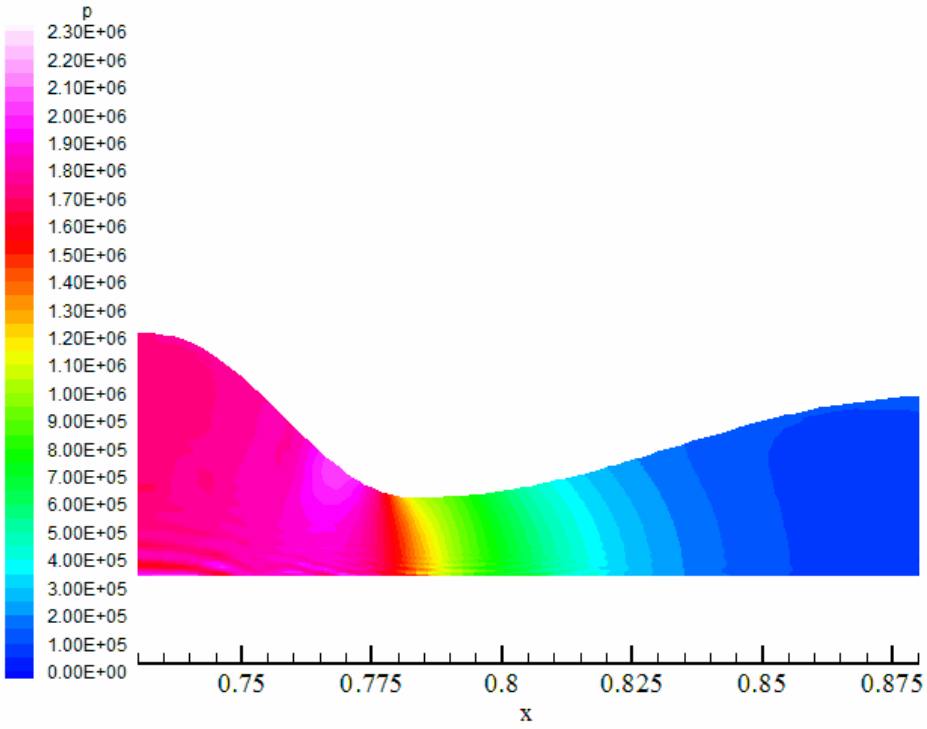

Fig.8. Pressure contours in the nozzle.

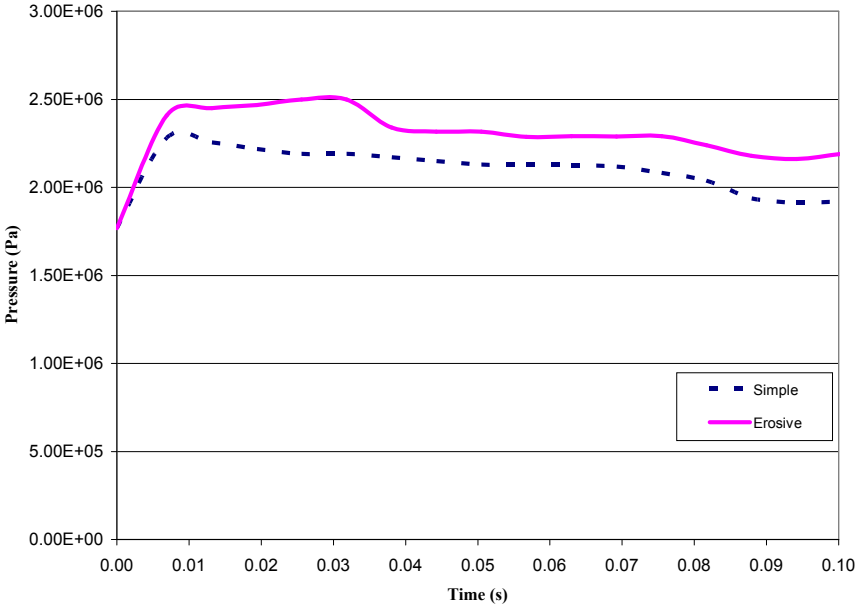

Fig. 9. Comparison of head-end pressure versus time with and without erosive burning.

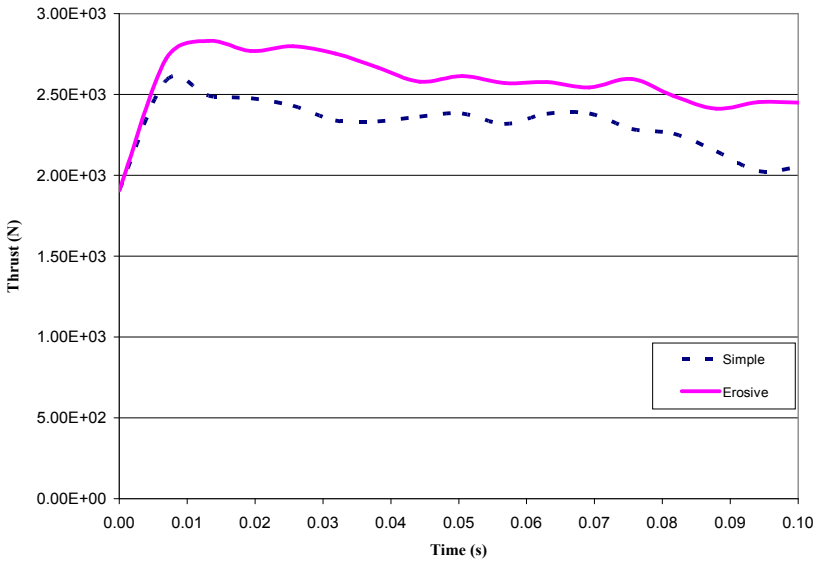

Fig. 10. Comparison of thrust versus time with and without erosive burning.

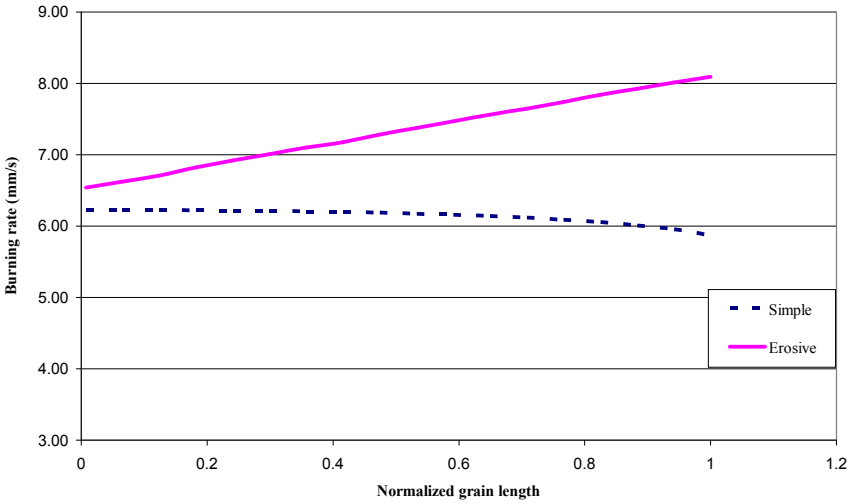

Fig. 11. Comparison of burning rate versus grain length with and without erosive burning.

The performance of a rocket propellant is often described by its specific impulse, I_{sp} which is the instantaneous impulse of the rocket per unit weight flow rate of the propellant

$$I_{sp} = \frac{F}{g\dot{m}} \tag{14}$$

where F is the thrust force, $\dot{m}$ is the mass flow rate of the propellant, g is the standard acceleration of gravity. Higher specific impulse means better performance. Solid propellants typically have an I_{sp} in the range of 100 to 300 s. Fig. 12 compares I_{sp} for simple and erosive burning rates. As seen, the specific impulse for erosive burning is lower than that for simple burning. This is an example of one of the undesirable characteristics of erosive burning.

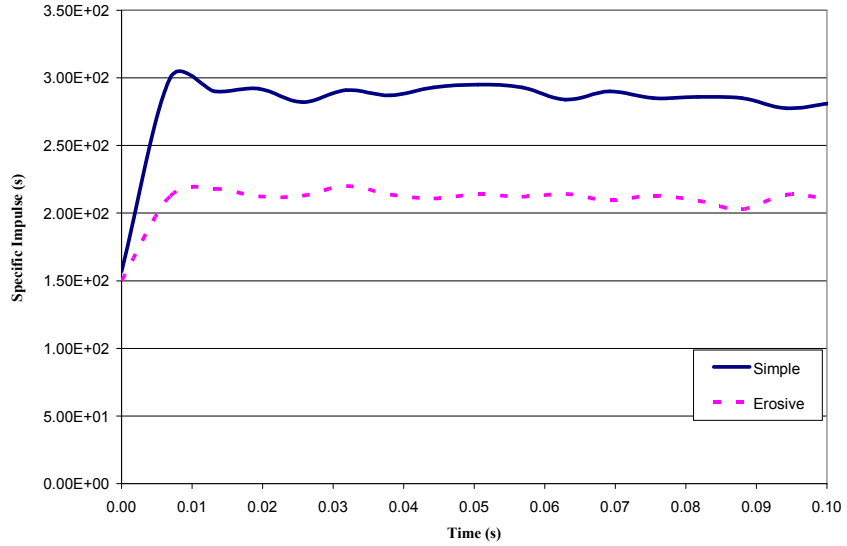

Fig. 12. Comparison of specific impulse versus time with and without erosive burning.

Fig. 13 shows axial velocity as a function of axial position along the grain at time t=0.01s. Axial velocity due to erosive burning is higher than that obtained by simple burning. One should note that in this paper we study transient burning of a typical solid rocket motor, however during the later stages of simulated burn, the velocity for simple burning case will be slightly higher due to the fact that the port diameter will be smaller.

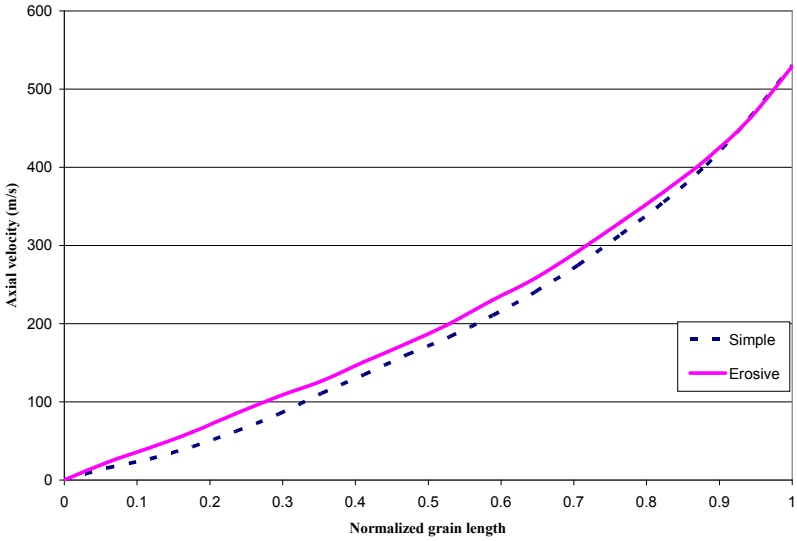

Fig. 13. Port centerline axial velocity versus grain location with and without erosive burning.

5- Conclusion

The start-up transient internal ballistic of a SRM with cylindrical grain is numerically simulated. Governing equations are two dimensional Euler equations and are solved using the MacCormack explicit finite difference scheme. Discharge from reservoir and nozzle flow test cases showed that the correct steady solutions are obtained with shock capturing capability. Two burning rate laws were used to compare simple burning and erosive burning. After obtaining a validated code for transient and steady-state solutions, ballistic calculations of a generic solid rocket motor was performed. Erosive burning increases the chamber pressure and thrust during the early portion of burning for the particular motor.

References

1- Greatrix, D.R., and Gottlieb, J.J., "Quasi steady analysis of the internal ballistics of SRMS," Canadian Aeronautical and Space Journal, Vol. 33, pp. 61-71, 1987.
2- Langherny, M.T., "Acceleration effects in solid propellant rocket motors, " AIAA Paper, 86-1577, 1986.
3- Sabnis, J., Gibeling, H.J., "Calculation of SRM internal flow field using an implicit Navier-Stokes procedure," AIAA Paper, 85-1626, 1985.
4- Sabnis, J., Gibeling, H.J., "Navier-stokes analysis of two and three dimensional flow field in SRMs with segment joints," AIAA Paper, 89-3319, 1989.
5- Williams, A., Combustion Theory, Benjamin & Cummings Publishing, 1985.
6- Razadan, M.K., and Kuo, K.K., "Erosive burning study of composite solid propellant by turbulent boundary-layer approach," AIAA Journal, Vol. 17, pp. 1225-1233, 1989.
7- Gordon, J.C., Duterque,J., and Lengelle, G., "Erosive burning in solid propellant motors," Propulsion and Power, Vol. 9, pp. 806-811, 1993.
8- Bulgakov, K., and Karpov, I., "Numerical studies of solid propellant erosive burning, " Propulsion and Power, Vol. 9, pp. 812-818, 1993.
9- Mukunda, H.S., and Paul, P.J., "Universal behavior in erosive burning of solid propellant," Combustion and Flame, Vol. 109, pp. 224-236, 1997.
10- Sutton, G.P., and Biblarz, O., Rocket Propulsion Elements, John Wiley & Sons, Inc., 2001.
11- Hirsch, C., Numerical Computation of Internal and External Flows, John Willey & Sons Inc., 1990.
12- Tinaztepe, H.T., and Akmandor, I.S., "Unsteady internal ballistic calculations of solid rocket motors," Journal of Propulsion and Power, Vol. 8, pp. 1125-1128, 1990.